Deformation induced martensite transformation in chemically heterogeneous austenite A 3D molecular dynamics study

Chai, Jun; Liu, Shichun; Dong, Haokai; Wang, Junsheng; Yang, Zhigang; van der Zwaag, Sybrand; Chen, Hao

DOI
10.1016/j.actamat.2025.121660

Publication date
2026

Document Version
Final published version

Published in
Acta Materialia

Acta Materialia 302 (2026) 121660

Contents lists available at ScienceDirect

Acta Materialia

journal homepage: www.elsevier.com/locate/actamat

Full length article

Deformation induced martensite transformation in chemically heterogeneous austenite: A 3D molecular dynamics study

Jun Chai [a,b], Shichun Liu [b], Haokai Dong [c], Junsheng Wang [a], Zhigang Yang [b], Sybrand van der Zwaag [b,d], Hao Chen [b,e,*]

[a] State Key Laboratory of Metallic Materials for Marine Equipment and Applications, Beijing, China
[b] Key Laboratory of Advanced Materials of Ministry of Education, School of Materials Science and Engineering, Tsinghua University, Beijing 100084, China
[c] State Key Laboratory of Advanced Marine Materials, Ningbo Institute of Materials Technology and Engineering, Chinese Academy of Sciences, Ningbo 315201, China
[d] Faculty of Aerospace Engineering, Delft University of Technology, Delft, the Netherlands
[e] Institute for Materials Research, Tohoku University, 2-1-1 Katahira, Aoba-ku, Sendai, 980-8577, Japan

ARTICLE INFO

Keywords:
Steel
Deformation-induced martensitic transformation
Chemical boundary engineering
Mechanical property
Molecular dynamics

ABSTRACT

This study employs 3D molecular dynamics simulations to investigate deformation-induced martensitic transformation (DIMT) in both chemically homogeneous and heterogeneous austenite grains, with particular emphasis on the distinctive role of chemical boundaries. Our findings reveal three fundamental differences between chemical boundaries and conventional interfaces: (i) they do not serve as nucleation sites for martensite formation, (ii) they effectively arrest propagating martensite, yet (iii) they exhibit negligible influence on stacking fault transmission. In the Fe-Ni model system, we demonstrate that DIMT behavior in compositionally graded core-shell austenite grains is predominantly governed by local Ni concentration, where increased Ni content significantly enhances phase stability. These insights demonstrate that precisely engineered chemical heterogeneities offer an effective pathway for controlling DIMT behavior, providing a novel paradigm for designing next-generation steels containing retained austenite with tunable mechanical properties.

1. Introduction

Metastable austenite significantly enhances the mechanical performance of advanced high-strength steels [1,2], primarily by improving strain hardening through deformation-induced martensitic transformation (DIMT) of retained austenite (RA) [3,4]. This mechanism has been successfully utilized in various steel families, including Transformation-Induced Plasticity steels [5], Quenching and Partitioning steels [6,7], carbon-free bainitic steels [8], and medium-manganese steels [9]. As a result, the mechanical stability of RA grains, which governs DIMT behavior, plays a critical role in determining the overall mechanical properties of these steels.

It has been well recognized that the mechanical stability of RA is dependent on various factors, including chemical composition [1,2], grain size [3], crystallographic orientation [4], and neighboring environments etc. [5–10]. Among these factors, chemical composition is one of the most critical factors that can influence the stability of RA both thermally and mechanically. In conventional steels, the chemical composition is typically assumed to be homogeneous within each individual grain, even though it may vary between grains due to solute segregation and local partitioning [11]. Recently, we [11] have introduced the concept of Chemical Boundary Engineering (CBE) to tailor the microstructure and achieve the enhanced mechanical performance in steels. The chemical boundary refers to a sharp chemical discontinuity that occurs without a change in crystal structure or crystal orientation, distinguishing it from well-defined phase boundaries and grain boundaries. They intentionally created chemical heterogeneities and thus chemical boundaries via flash heating of medium-Mn steels into a fully austenitic state. It was found that these intragranular chemical boundaries can effectively arrest martensitic transformation upon quenching, thereby substantially altering the overall transformation behavior. This phenomenon bears resemblance to the inhibitory effects observed at conventional grain boundaries and phase boundaries, albeit through different mechanisms. While grain and phase boundaries primarily derive their functionality from crystallographic orientation discontinuities (with potential secondary chemical variations), the chemical boundary is uniquely characterized by a pure compositional gradient without crystallographic orientation change. Subsequent work by Wan

* Corresponding author.
E-mail address: hao.chen@mail.tsinghua.edu.cn (H. Chen).

https://doi.org/10.1016/j.actamat.2025.121660
Received 1 July 2025; Received in revised form 27 September 2025; Accepted 21 October 2025
Available online 22 October 2025

et al. advanced the CBE concept by creating chemically heterogeneous RA grains with a high Mn-containing shell and a low Mn-containing core in medium Mn steels [12]. They discovered that the Mn compositional gradient at the core-shell interface serves as a barrier to martensitic nucleation at the single-grain level. Consequently, such engineered RA grains exhibit progressive DIMT across an extended strain range, contrasting with the abrupt transformation behavior of chemically homogeneous RA grains. These findings suggest that CBE has considerable potential for optimizing microstructure and properties in advanced steels. However, the fundamental mechanisms by which chemical boundaries govern martensitic transformation in chemically heterogeneous austenite remain poorly understood. Critical questions regarding whether chemical boundaries primarily affect martensite nucleation, propagation, or both remain unanswered, and they are challenging to resolve using conventional experimental techniques.

Molecular Dynamics (MD) simulations have demonstrated significant advantages in elucidating the atomic-scale mechanisms of DIMT. Previous MD studies have extensively explored the influence of various defects, such as stacking faults [13], twin boundaries [13,14], dislocations [15,16], grain boundaries [17,18], and phase interfaces [19], on martensite nucleation. Unlike topological defects, chemical boundaries do not induce significant lattice distortions or stress concentrations, and their impact on martensitic transformation is expected to differ fundamentally from that of defects. In this study, MD simulations are employed to investigate the mechanistic role of chemical boundaries in martensitic transformation behavior. Emphasis is placed on the kinetics of martensitic transformation in chemically heterogeneous austenite grains with core-shell structure. The effects of Ni concentration and shell thickness on martensite nucleation are addressed. The competitiveness between the chemical driving force and local stress-induced driving force on martensite nucleation is discussed.

2. Simulation details

The material to be considered in our MD simulation is the binary Fe-Ni system, which is suitable for MD studies given the accuracy of the interatomic potentials. The Ni-containing system is also relevant for various types of high-strength steels, such as stainless steels and maraging steels. The model consists of a single spherical austenite grain which has a compositional core-shell structure embedded in a pure iron BCC matrix. The crystallographic orientations of the ferritic matrix and the austenite particle, as well as the straining direction, are fixed in a manner that promotes DIMT. The only variables in the simulations are the compositions of the core and shell, as well as the thickness of the shell. The chemical boundary between the core and shell is characterized by a stepwise transition in composition perpendicular to the boundary., occurring over a distance comparable to the scale of a single atomic layer, i.e. without a proper concentration gradient.

The dimensions of the supercell are $35.9 \times 35.9 \times 35.9\ \mathrm{nm}^3$ in the x-, y-, and z-directions, parallel to $[100]_{\mathrm{bcc}}$, $[010]_{\mathrm{bcc}}$, and $[001]_{\mathrm{bcc}}$, respectively. The outer radius of the austenite grain was fixed at 14 nm. The relative rotation from BCC to FCC is described by the quaternion [0.18, −0.13, −0.18, 0.96]. Correspondingly, the FCC crystallographic directions in the Cartesian coordinate system are: $[100]_{\mathrm{fcc}} \approx$ [0.90, 0.30, −0.31], $[010]_{\mathrm{fcc}} \approx$ [−0.39, 0.87, −0.30], and $[001]_{\mathrm{fcc}} \approx$ [0.18, 0.39, 0.90]. The method developed by Dai and Zhang [20] was used to achieve a low-energy configuration for the incoherent interface between the FCC particle and the BCC matrix. The OVITO software [21] was utilized to visualize the DIMT process, and the PTM (Polyhedral Template Matching) algorithm [22] was employed to classify the structure types of atoms in the system. The total number of atoms in each simulation was about 4 million. The nomenclature adopted to represent the various systems explored, CXSY, succinctly conveys the compositional details of the core-shell structure: 'C' denotes the core, 'S' denotes the shell, and 'X' and 'Y' represent the atomic fractions of Ni in the core and shell regions, respectively. Notably, homogeneous models are also described using the uniform format CXSX. Fig. 1 shows an example of three-dimensional (3D) core-shell structural schematics of C0S40, with a shell thickness of 7 nm and a particle radius of 14 nm.

To simulate the DIMT, MD simulations were employed using the Large-scale Atomic/Molecular Massively Parallel Simulator (LAMMPS) code [23]. A second nearest-neighbor modified embedded-atom method (2NN MEAM) potential for the Fe–Ni system, developed by Wu et al. [24], was employed to describe atomic interactions and local compositional evolution. All simulations, including relaxation and tensile deformation, were conducted at 300 K to represent typical room-temperature conditions and focus on deformation-induced rather than thermally-driven phase transformation. The NPT ensemble was used to control the temperature and pressure of the simulation system. The simulation cell was subjected to tensile deformation along the $\boldsymbol{x}$-direction at a strain rate of $1 \times 10^9\ s^{-1}$. The maximum engineering strain imposed in the calculations was $\varepsilon = 7.0\%$.

3. Results and discussions

3.1. DIMT in chemically homogeneous austenite grain

Figs. 2 and 3 illustrate the progression of DIMT within a homogeneous austenite grain as a function of strain in 3D and 2D Observations were conducted along the $[110]_{fcc}$ direction. **Supplementary Movie M1** provides a detailed 3D visualization of the stacking fault formation and martensitic transformation processes in the C0S0 system. The series of subplots in Fig. 3 are labeled from **(a0) to (a5), (b0)** to **(b5)**, and **(c0)** to **(c5)**, corresponding to different Ni concentrations in the austenite grains: C0S0, C5S5, and C10S10, respectively. The interface between the austenite and the matrix is delineated by a thin white circle with dashed lines. In Fig. 3**(a0, b0, c0)**, reflecting the unstrained starting conditions, Ni atoms are depicted as blue points, demonstrating their uniform distribution. The evolution of DIMT in the C0S0 alloy from a tensile strain of $\varepsilon = 3.0\%$ to $\varepsilon = 4.6\%$ is depicted in Fig. 3**(a1)** to **(a5)**. During strain loading, stacking faults (HCP, indicated in red) initially form at the α/γ interface, grow into the particle, and gradually develop into a network. At higher strains, martensite (BCC, shown in blue) typically initiates at the α/γ interface, although it may also emerge at junctions within the stacking fault network, as illustrated in Fig. 3**(a5)**. At higher Ni concentrations, the minimal strain required to form either stacking faults or martensite increases, and their formation rate decreases, as evidenced by comparing Fig. 3**(a, b and c).** For the C10S10 case, only a small amount of martensite is present at $\varepsilon = 4.6\%$, as shown in Fig. 3**(c5)** and **Supplementary Movie M2**. Simulations with Ni concentrations exceeding 10 atomic percent (not shown here) indicate that martensite transformation does not occur even when the system is strained to $\varepsilon = 7.0\%$.

The evolution of the stacking fault and martensite fractions in chemically homogeneous austenite grains with different Ni content is summarized in Fig. 4**(a** and **b)**. It should be noted that at some stages of the transformation, the local crystal structure of some atoms in the transformed region cannot be classified with certainty and is excluded from the analysis. The fraction of unaccountable atoms ranges from 0 % to 20 % depending on the deformation structures formed. As a result, the sum of the stacking fault and martensite fractions does not reach 100 % even when the austenite grain is (almost) fully transformed. The transformation behavior of the typical homogeneous C0S0 model can be characterized by several distinct stages: (1) In the first stage, stacking faults form first and propagate extensively into the austenite grain. Although the 2D projections in Fig. 3 suggest that some stacking faults appear to terminate arbitrarily within the austenite grain, a more comprehensive 3D analysis of the situation depicted in Fig. 2 revealed that this apparent random termination is actually due to the SFs intersecting with other stacking faults in non-parallel planes. Martensite was found to nucleate at the matrix-particle interface and grows

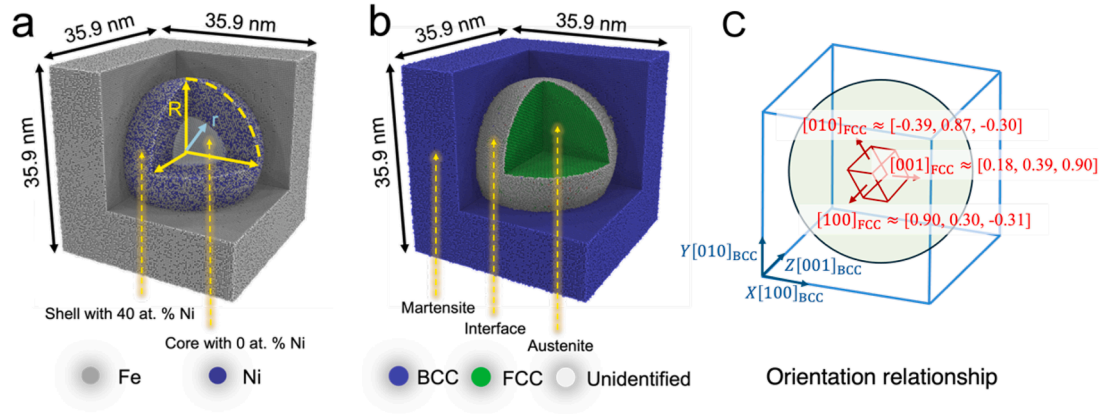

Fig. 1. Schematics of core-shell structure of C0S40 in 3D. Subplot **(a)** exemplifies the Ni distribution among core-shell structure, **(b)** delineates the phase distribution and **(c)** the orientations of the BCC matrix and the initial FCC with respect to each other.

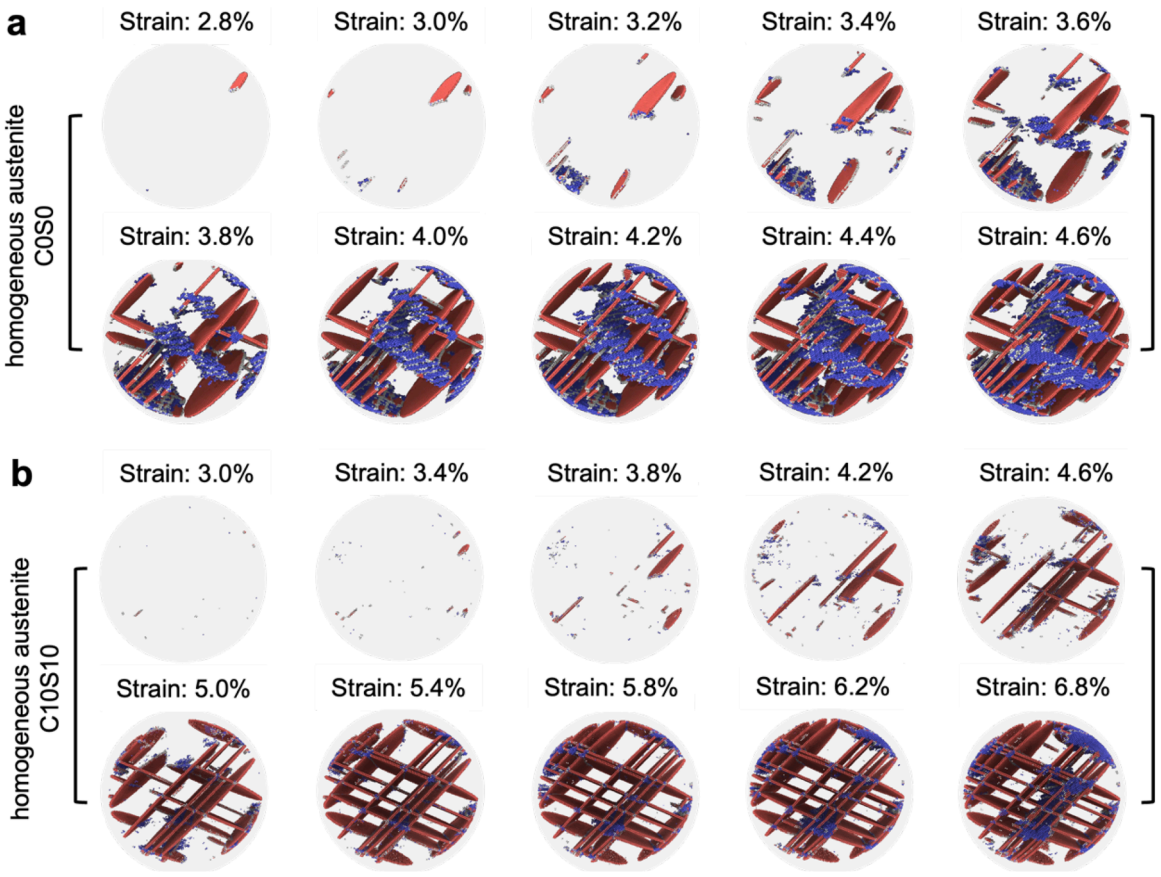

Fig. 2. Atomic-scale DIMT evolution in 3D for homogeneous austenite C0S0 and C10S10. Grey spheres represent austenite grain regions. To enhance clarity in visualizing the intragranular evolution, atomic data near the α/γ interface were omitted to reduce noise. Red indicates stacking faults, while blue denotes martensitic regions.

predominantly in its vicinity; (2) In the second stage, both martensite and stacking faults grow concurrently, and the fraction of stacking fault reaches its maximum value; (3) In the final stage, martensite continues to expand, consuming some of the existing stacking faults, which leads to a reduction in the stacking fault fraction. The nucleation of both stacking faults and martensite is progressively postponed as the Ni concentration increases in the homogeneous austenite. This suppression effect is more pronounced for martensite nucleation than for stacking fault formation, as evidenced by the comparison between Fig. 4**(a** and **b)**. When the Ni content in homogeneous austenite reaches 17 %, stacking fault formation is significantly suppressed and almost ceases, and detectable martensite formation occurs at strains beyond 7 %.

3.2. *DIMT in chemically heterogeneous austenite*

For the case of chemically heterogeneous austenite, two different scenarios are considered: (i) Ni-free core and Ni-rich shell, (ii) Ni-rich core and Ni-free shell. In the first scenario, the Ni concentration in the shell varies from 10 to 40 at %, while it is fixed at 0 in the core, resulting in C0S10, C0S20, C0S30, and C0S40. In the second scenario, the Ni

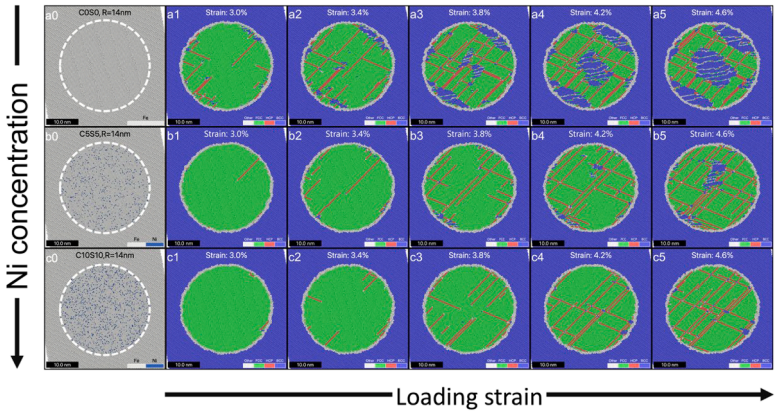

Fig. 3. Atomic-scale DIMT evolution in slices across different systems. Panels **(a0-c0)** show the elemental distributions within homogeneous austenitic systems (C0S0, C5S5 and C10S10). The displayed plane is $(110)_{fcc}$ plane through the center of the austenitic sphere. The subsequent panels from **(a1-a5)** to **(c1-c5)** demonstrate the progression of DIMT at incremental strains of 3.0 %, 3.4 %, 3.8 %, 4.2 %, and 4.6 % for each respective system. Red marks the stacking faults, and blue marks the martensitic regions.

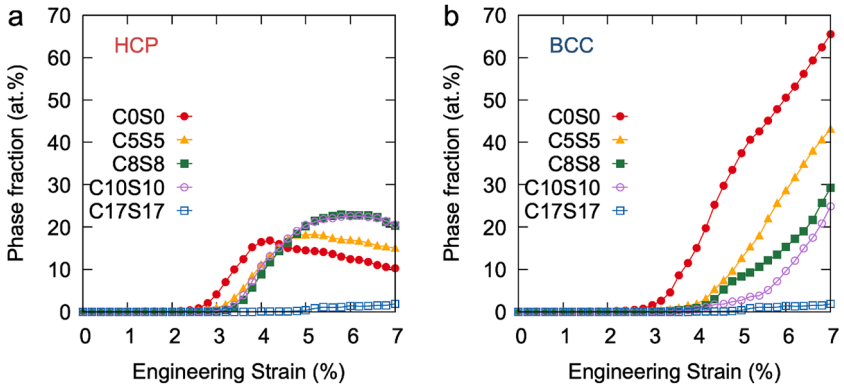

Fig. 4. Phase evolution with engineering strain in homogeneous systems. **(a)** HCP phase, **(b)** BCC phase.

concentration in the core varies from 10 to 40 at %, while it is fixed at 0 % in the shell, resulting in C10S0, C20S0, C30S0, and C40S0. Fig. 5**(a)** and **(b)** show a quasi-3D plot of the structure evolution as a function of strain for the C0S40 and C40S0 systems. The full 3D images can be found in **Supplementary Movie M3** and **M4**. The simulation results for C0S10, C0S20, C0S30, and C0S40 in Fig. 6 demonstrate that as the Ni concentration in the shell increases, the formation mechanism of stacking faults undergoes significant changes. Stacking faults are observed to initiate from the α/γ interface at $\varepsilon = 3.4\%$ for C0S10, as shown in Figs. 6**(a2)** and 7**(a)**. In contrast, no stacking fault is formed at the α /γ interface within the strain range of interest for the C0S40 model, as illustrated in Fig. 6**(d1** to **d5)**. The generation of stacking faults shifts from the α /γ interface to the core region, as depicted in Fig. 6**(a2** and **d5)**. This shift is attributed to the stacking fault energy, which increases linearly with Ni concentration. The Ni-free core region in C0S40 exhibits a lower SFE, promoting stacking fault nucleation, whereas the high Ni content in the shell near the α/γ interface elevates the SFE, suppressing fault formation at this boundary. The detailed 3D results in Fig. 5**(a)** reveal that the formation process of stacking fault is accompanied by martensite nucleation in the Ni-lean core region.

Fig. 8 presents the MD simulations of DIMT in austenite with a Ni-rich core and a Ni-free shell, including C10S0, C20S0, C30S0, and C40S0. Similar to the homogeneous cases, stacking faults originate from the α/γ interface in the Ni-rich core cases. Unlike the Ni-rich shell cases, stacking fault formation still occurs in the core despite high Ni concentrations, as shown in Fig. 9**c**. However, the number of stacking faults in the core decreases with increasing Ni concentration, as evidenced by comparing C10S0 and C40S0, which is exhibited in Fig. 8**(a5** and **d5)**. Although stacking faults still interact with each other within the core region during tensile loading, martensite nucleation rarely occurs at these interactions (see yellow, green, and blue curves in Fig. 9**(d)**). Instead, martensite nucleation is restricted to the (Ni-free) shell region, as shown in Fig. 5**(b)**. Interestingly, the presence of chemical boundaries alters the martensite nucleation mechanism in heterogeneous austenite. As shown in Figs. 6 and 8, martensite grows almost exclusively in low-Ni regions and arrests at chemical boundaries, regardless of whether the system features Ni-rich shells or Ni-rich cores. These findings suggest that the chemical driving force arising from concentration gradients exerts a dominant influence on martensite nucleation than the phase boundaries, consequently diminishing the nucleation priority at interfaces. For instance, in shell-rich systems, martensite can only nucleate and grow within grain interiors, as demonstrated in Fig. 5**(a).** On the other hand, the local growth behavior of martensite in heterogeneous austenite is primarily governed by the local composition. Higher Ni concentrations lead to delayed martensite nucleation, as evidenced in Figs. 7**(b-d)** and 9**(b-d)**. Classical martensite transformation theory states that martensite growth can only be arrested at defects such as grain boundaries or phase interfaces. However, the present results suggest that chemical boundaries, lacking any topological misfit in their structure, can also exhibit strong shielding effects on martensite growth, although martensite neither initiates from the chemical boundary itself nor is promoted by it.

In contrast to their effect on martensite transformation, the MD simulations show that chemical boundaries exert a minimal influence on the propagation of stacking faults. Stacking faults can readily traverse chemical boundaries even in the presence of significant compositional

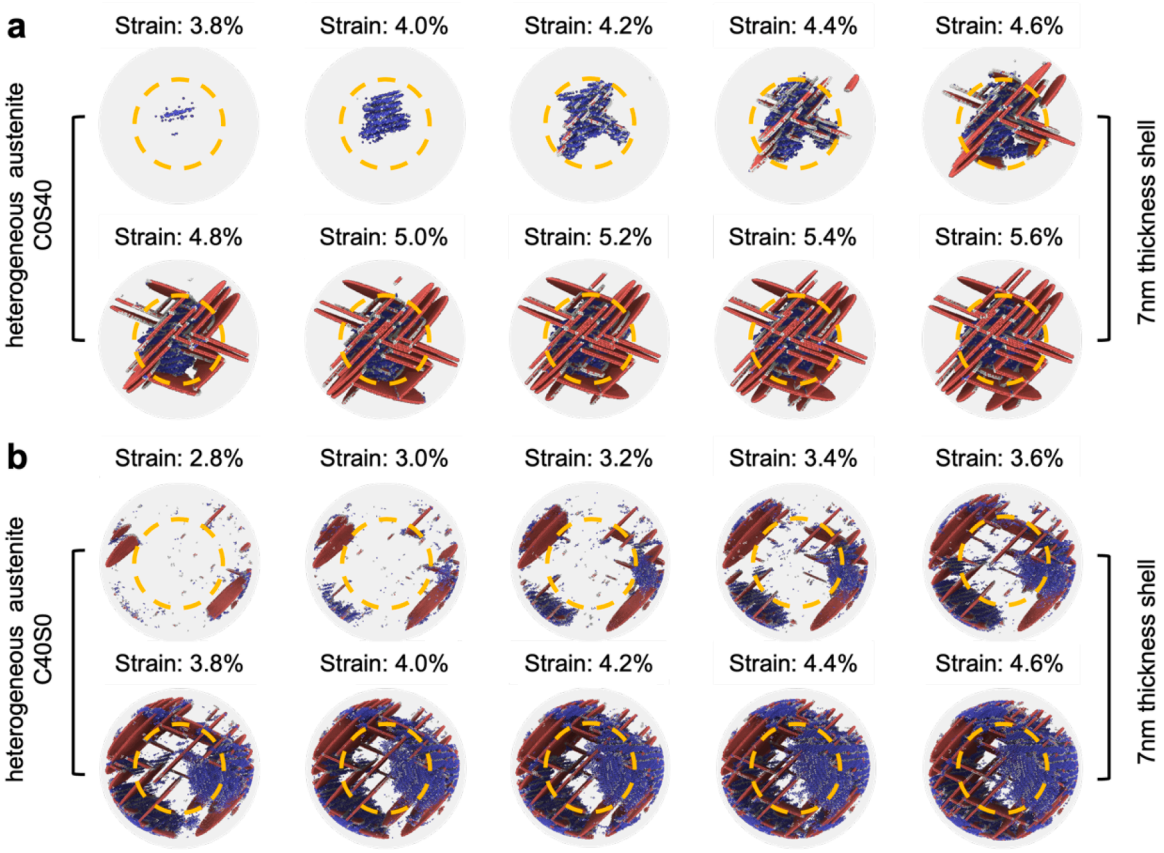

Fig. 5. Atomic-scale DIMT evolution in 3D of heterogeneous austenite C0S40 and C40S0. The grey spheres mark the austenite grains, and the yellow dashed circles mark the chemical boundaries.

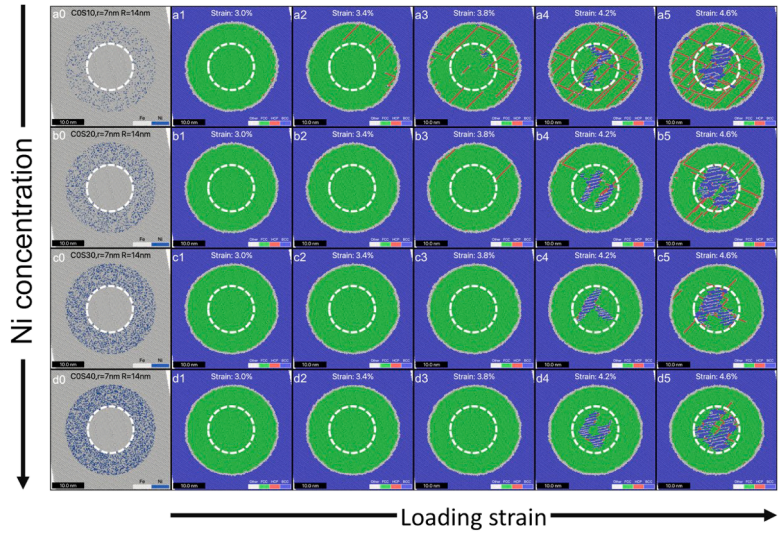

Fig. 6. Atomic-scale DIMT evolution in slices across different systems. Panels (a0-d0) show the elemental distributions within rich-shell austenitic systems (C0S10, C0S20, C0S30 and C0S40). The displayed plane is the $(110)_{fcc}$ plane through the center of the austenitic sphere. The subsequent panels from **(a1-a5)** to **(d1-d5)** demonstrate the progression of DIMT at incremental strains of 3.0 %, 3.4 %, 3.8 %, 4.2 %, and 4.6 % for each respective system.

differences.

The results above demonstrate the critical role of chemical composition in the shell or core in modifying DIMT in chemically heterogeneous austenite. It is naturally anticipated that the size of the shell or core may also significantly influence this process. To explore this, new core-shell models were constructed, where the core region maintains an identical structure and composition while the shell shares the same composition but varies in thickness. These models were used to investigate the effects of shell thickness on martensitic transformation. To clarify the shell thickness, a critical strain (ε_c) was defined as the overall tensile strain at which martensitic transformation occurs, i.e., when the martensite (BCC) fraction reaches 1.5 % of the total number of atoms. This quantity was measured separately in both the core and shell regions. As shown in Fig. 10**(a)**, ε_c in the core region remains consistent

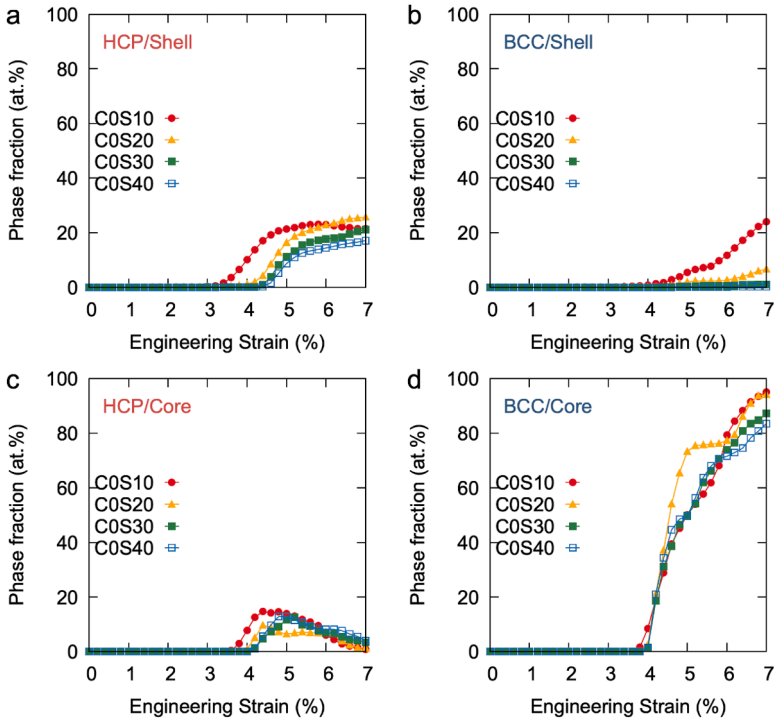

Fig. 7. Phase evolution with engineering strain in heterogeneous systems (Ni rich in shell). **(a)** HCP phase in shell, **(b)** BCC phase in shell, **(c)** HCP phase in core, **(d)** BCC phase in core.

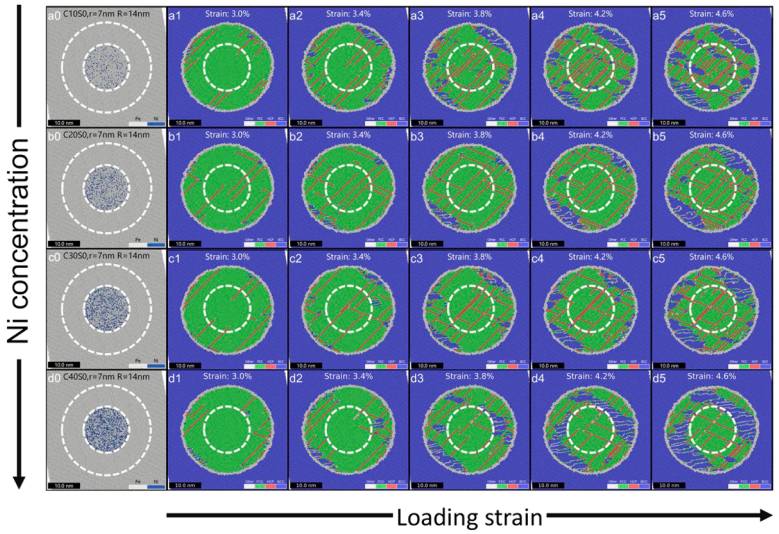

Fig. 8. Atomic-scale DIMT evolution in slices across different systems. Panels **(a0-d0)** show the elemental distributions within rich-core austenitic systems (C10S0, C20S0, C30S0 and C40S0). The displayed plane is $(110)_{fcc}$ plane through the center of the austenitic sphere. The subsequent panels from **(a1-a5)** to **(d1-d5)** demonstrate the progression of DIMT at incremental strains of 3.0 %, 3.4 %, 3.8 %, 4.2 %, and 4.6 % for each respective system.

across different configurations and shows no dependence on shell thickness. In contrast, ε_c in the shell region is strongly influenced by shell thickness. Specifically, in the C0S10 configuration, martensite nucleation preferentially initiates in the shell when the thickness ranges from 3 nm to 7 nm (see Fig. 10a1), whereas at 9.5 nm, nucleation shifts to the core region. For configurations with higher Ni gradients (C0S20, C0S30, and C0S40), increasing shell thickness leads to a pronounced delay in martensite nucleation. Notably, in C0S40 as shown in Fig. 10**a4**, no martensite nucleation occurs at shell thicknesses of 7 nm or 9.5 nm.

In heterogeneous scenarios, the local shear strain within austenite grains is not uniform, thus altering the stress-driven driving force for martensitic transformation. The size-dependent shift in nucleation site arises from the interplay between shell thickness and local stress distribution. For thin shells (e.g., 3 nm in C0S10), the reduced thickness leads to a higher stress concentration and constrained deformation, elevating the local shear strain in the shell region compared to thicker shells (5–9.5 nm), where the stress is more uniformly distributed across the core-shell interface. Fig. 10**(b1-b4)** illustrates the evolution of average local shear strain in both core and shell regions with increasing tensile strain for systems with varied chemical compositions and shell thicknesses. The local shear strain values were calculated using OVITO's Atomic Strain/Elastic Strain function, which fits a local deformation gradient for each atom based on its neighbors relative to the reference (undeformed) configuration and then computes the von Mises shear

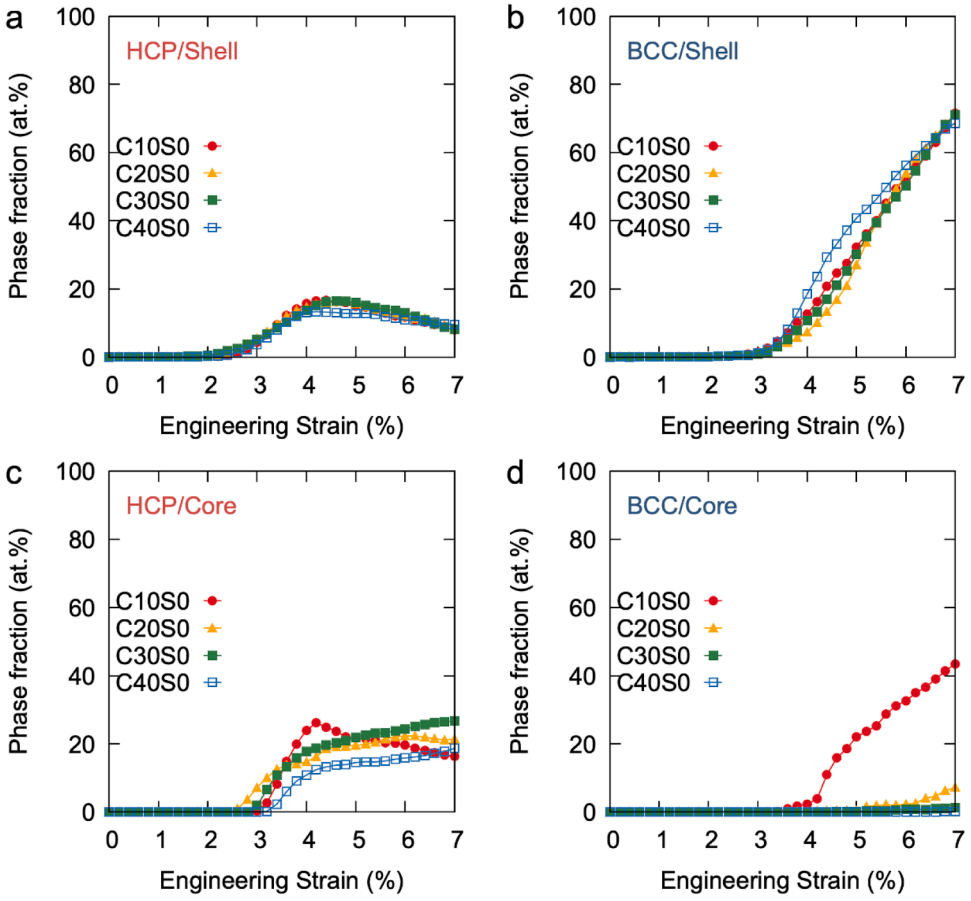

Fig. 9. Phase evolution with engineering strain in heterogeneous systems (Ni rich in core). **(a)** HCP phase in shell, **(b)** BCC phase in shell, **(c)** HCP phase in core, **(d)** BCC phase in core.

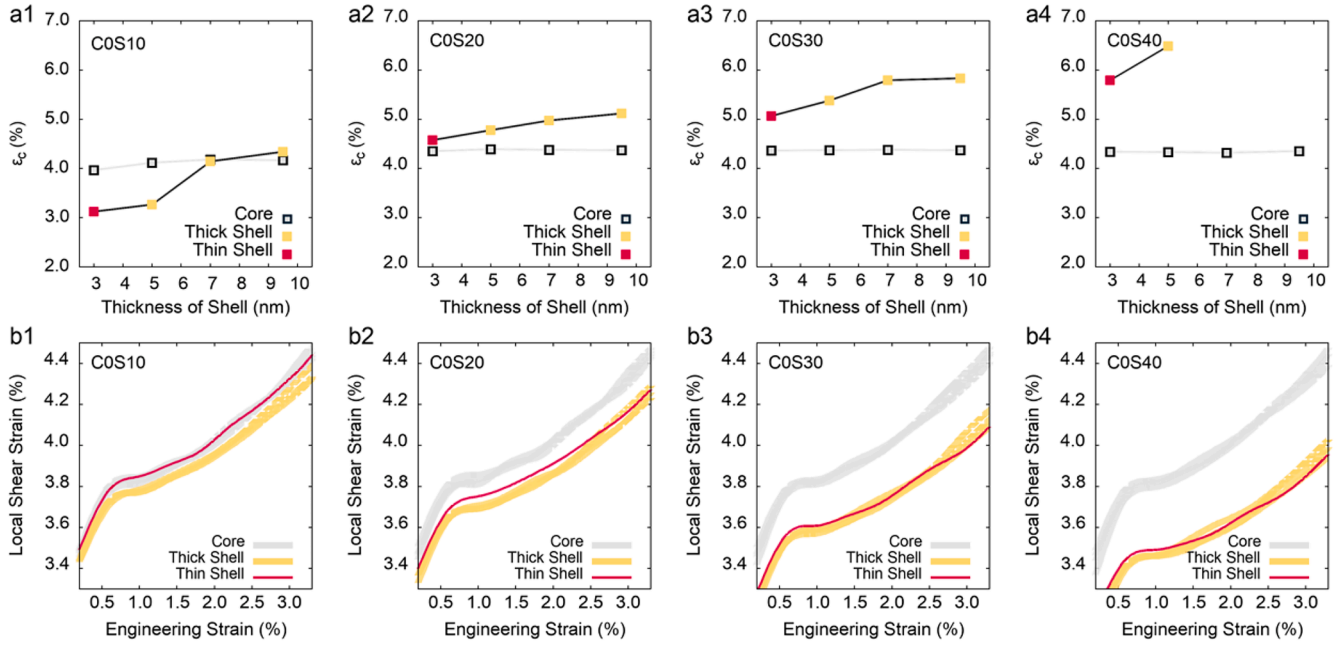

Fig. 10. **(a)** Dependence of critical strain ε_c on shell thickness for core-shell nanoparticle (C0SY) systems. **(b)** Evolution of local shear strain in the core and shell regions as a function of applied engineering strain. Thin shell corresponds to 3 nm thickness; thick shell corresponds to 5–9.5 nm thickness.

strain from the deviatoric part of the resulting Green–Lagrangian strain tensor.

First, given that the core regions in all models share identical chemical compositions and dimensions, their local shear strain evolution follows a consistent trend. In contrast, the average local shear strain in the shell region decreases progressively with increasing Ni concentration. This trend aligns with our earlier finding that elevated Ni concentrations suppress martensite nucleation in the shell, while the relatively higher local shear strain levels in the core facilitate preferential nucleation in this region. For thinner shells, the higher local shear strain is a geometric effect, where the constrained geometry amplifies stress accumulation, overcoming the chemical suppression in low Ni systems like C0S10. It should be noted that shell thickness also significantly influences local shear strain distribution. Comparative analysis reveals that thinner shells (e.g., 3 nm) maintain higher local shear strain levels than their thicker counterparts (5–9.5 nm), particularly in systems with relatively low Ni concentrations (C0S10 and C0S20). In the C0S10 system specifically, the local shear strain level in the shell (red curve, Fig. 10**b1**-**b4**) becomes comparable to or even exceeds that of the core (grey curve, Fig. 10**b1**-**b4**), eliminating the core's preferential nucleation advantage and consequently shifting martensite nucleation sites toward phase interfaces, as illustrated in Fig. 10**(a1)**. In contrast, as Ni concentration increases (C0S20-C0S40), the chemical driving force (via elevated SFE) becomes dominant, suppressing shell nucleation regardless of thickness, as the local shear strain remains insufficient to trigger transformation. These findings highlight a competitive interplay between chemical driving forces and strain-induced driving forces in martensite nucleation, with the simulation results suggesting the potential dominance of chemical driving forces in high Ni systems, while size effects prevail in low Ni, thin-shell configurations.

3.3. General discussion

The critical strain ε_c for DIMT initiation is predominantly controlled by the Ni concentrations in both the shell and core regions, with shell thickness playing a secondary role. The relationship between ε_c and the Ni concentration is summarized in Fig. 11. All simulations were performed with a fixed chemical boundary position at $r = 7$ nm and a shell thickness of 7 nm, consistent with the configurations in Figs. 6 and 8. Two characteristics are identified. (i) Shell-driven transformation behavior (Fig. 11a). In the C0SY series (representative shell-rich models where martensite nucleation initiates in the core), increasing the Ni concentration in the shell from 0 to 10 at % progressively suppresses martensitic transformation in both the shell and core regions, resulting in a continuous rise in ε_c. This demonstrates that the martensitic transformation herein is primarily governed by the Ni concentration in the shell. (ii) Transition to core-controlled transformation. When the Ni concentration in the shell exceeds 10 at % (up to 30 at %), martensite nucleation shifts exclusively to the core region. Beyond this threshold, further increases in Ni concentration no longer affect the transformation process, causing ε_c to stabilize at a constant value. This identifies 10 at % Ni in the shell as a critical transition point for nucleation site switching. For the C20SY and C30SY models, the suppression effects on martensite nucleation become more pronounced, accompanied by the absence of a transition point within the investigated Ni concentration range, which underscores the critical role of Ni concentration in the shell in regulating martensitic transformation behavior.

Fig. 11**(b)** illustrates the correlation between Ni concentration in the core and ε_c in systems with fixed shell Ni content. The CXS0 series, representative of core-rich configurations, demonstrates that increasing core Ni concentrations substantially inhibits martensite nucleation within the core region (Fig. 9d). As the ε_c at the α/γ interface is lower than that within the austenite grain, increasing Ni concentration in the core has a marginal effect on the martensite nucleation within the austenite grain. Consequently, ε_c remains nearly constant. A similar trend is observed in the CXS10 models, where martensite nucleation also predominantly occurs at the interface. The higher ε_c values in these models indicate that martensite nucleation is further delayed compared to the CXS0 models. In contrast, the CXS20 system exhibits a composition-dependent nucleation transition. For core Ni concentrations below 10 at %, nucleation initiates preferentially within the core region, a characteristic of core-dominated transformation mechanisms. Beyond the critical threshold (approximately 10 at %), the nucleation site primarily shifts to the phase boundaries. Remarkably, the CXS30 models exhibit similar behavior to the C20SY and C30SY models, highlighting the critical role of Ni governing both nucleation site selection and strain threshold requirements for martensite transformation.

For all model conditions, a simple parameter $\Delta\varepsilon_c$ is introduced to determine the preferred location of martensite nucleation

$$\Delta\varepsilon_c = \varepsilon_c^{core} - \varepsilon_c^{shell} \tag{1}$$

where ε_c^{core} is the critical strain for martensite formation in the core, and ε_c^{shell} is that for the shell. Positive and negative values of $\Delta\varepsilon_c$ indicate whether the martensite preferentially nucleates in the shell or in the core, respectively. Fig. 12 illustrates the relationship between Ni concentration and the martensite nucleation preference site for systems in which the shell thickness is fixed at 7 nm (i.e., half the particle radius). Detailed data are provided in **Supplementary Fig. S1**. The martensite formation map features two distinct domains: (1) a blue-colored 'Shell first' region, indicating compositions where martensite nucleation

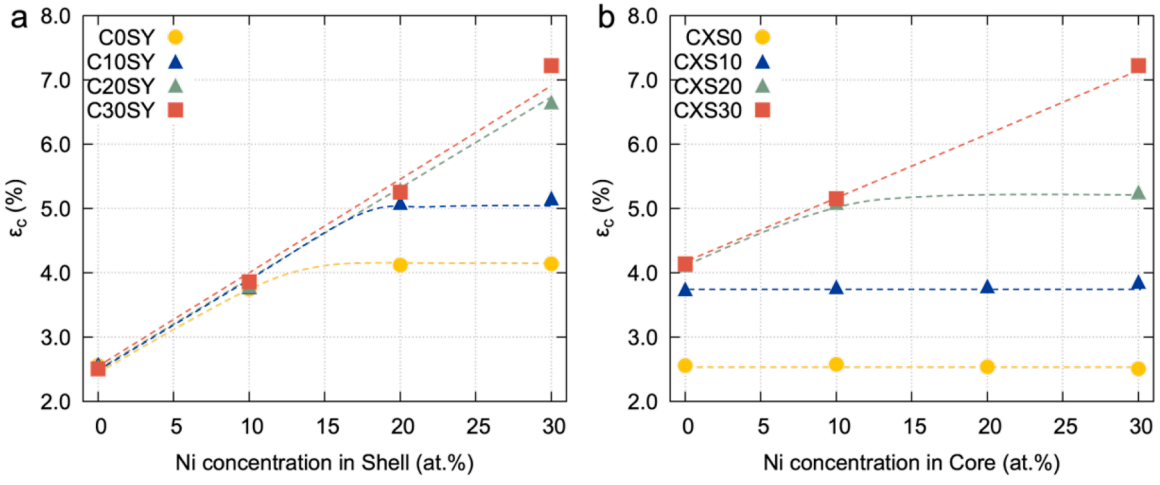

Fig. 11. Plot of ε_c as a function of Ni concentration in core and shell. **(a)** fixed Ni concentration in core, **(b)** fixed Ni concentration in shell.

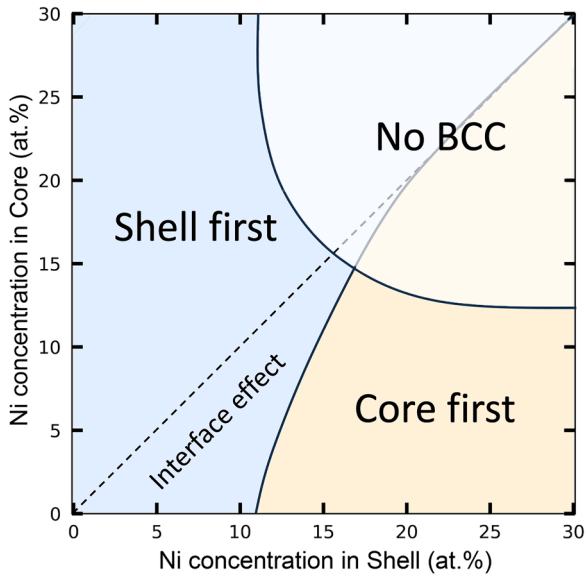

Fig. 12. The martensite formation map controlled by the Ni concentration in both shell and core. All simulations are performed at a fixed thick shell of 7 nm.

initiates in the shell region, and (2) a yellow-colored 'Core first' region, representing compositions favoring core nucleation. However, not all potential martensite nucleation sites proceed to develop into mature martensite. The third uncolored zone at high Ni levels in the core and shell corresponds to conditions where martensite formation does not measurably occur at a strain of 7 %. It needs to be pointed out that if the α/γ interfaces connecting the austenite grains to the matrix have not been present in the models, the 'Shell first' and 'Core first' zones will follow a symmetric diagonal (dashed line from C0S0 to C30S30), with the distinction being based entirely on the Ni concentration. However, the existence of the α/γ interface influences the nucleation process, making certain conditions more inclined to nucleate martensite from the shell region. It should be noted that, since the calculations were performed at 10 % Ni intervals, the positions of the separation lines between the various domains are necessarily approximate.

By analyzing the relationship between chemical composition distribution and preferred martensite nucleation sites, we propose a generalized framework for understanding deformation induced martensitic transformation in chemically heterogeneous austenite, which is of great practical importance for tailoring mechanical performance of high strength steels. This framework elucidates how compositional variations across core-shell structures drive distinct transformation behaviors, with α/γ interfaces promoting nucleation and high Ni concentrations suppressing it, potentially leading to transformation-free domains. The identified competition between interface-induced nucleation and composition-driven suppression not only governs martensite transformation in the Fe-Ni system studied here but is also applicable to other systems, such as Fe-Mn, providing broader insights into the mechanisms of martensitic transformation.

4. Conclusions

3D molecular dynamics simulations were employed to investigate deformation-induced martensitic transformation (DIMT) in both chemically homogeneous and heterogeneous austenite grains, with particular emphasis on the role of chemical boundaries in governing martensitic transformation. The results demonstrate that chemical boundaries exhibit fundamentally distinct behavior compared to conventional grain boundaries or phase interfaces. Specifically, these boundaries: (1) do not act as preferential nucleation sites for martensite formation, (2) effectively impede the propagation of locally formed martensite, and (3) show negligible influence on stacking fault propagation. In the Fe-Ni system studied here, the local DIMT behavior in core and shell regions is primarily governed by their respective Ni concentrations, with higher Ni content enhancing the stability of austenite. However, we anticipate that in systems like Fe-C, where carbon significantly alters both the chemical driving force and mechanical strength of austenite, martensitic transformation in core/shell regions may also be influenced by strain redistribution effects from neighboring regions. This work demonstrates that strategically introducing chemical heterogeneities within austenite grains provides an effective means to tailor DIMT behavior, offering a promising pathway for designing retained austenite (RA)-containing steels with optimized mechanical performance.

CRediT authorship contribution statement

Jun Chai: Writing – review & editing, Writing – original draft, Visualization, Validation, Software, Resources, Project administration, Methodology, Investigation, Formal analysis, Data curation. **Shichun Liu:** Formal analysis, Data curation. **Haokai Dong:** Writing – review & editing, Investigation, Formal analysis. **Junsheng Wang:** Writing – review & editing, Project administration, Funding acquisition. **Zhigang Yang:** Writing – review & editing, Supervision, Methodology, Formal analysis. **Sybrand van der Zwaag:** Writing – review & editing, Supervision, Methodology, Investigation, Formal analysis. **Hao Chen:** Writing – review & editing, Supervision, Methodology, Funding acquisition, Formal analysis, Conceptualization.

Declaration of competing interest

The authors declare that they have no known competing financial interests or personal relationships that could have appeared to influence the work reported in this paper.

Acknowledgements

H. Chen acknowlegdes financial support from the National Natural Science Foundation of China (grant No. 52525104), and Major Scientific and Technological Projects of Liaoning Province Innovation Consortium (grant No. 2023JH1/11200012). Z.G. Yang acknowledges financial support from the National Natural Science Foundation of China (grant No. 52171008).

Supplementary materials

Supplementary material associated with this article can be found, in the online version, at doi:10.1016/j.actamat.2025.121660.

References

[1] O. Matsumura, Y. Sakuma, H. Takechi, Enhancement of elongation by retained austenite in intercritical annealed 0.4C-1.5Si-0.8Mn steel, Trans. Iron Steel Inst. Jpn. 27 (1987) 570–579, https://doi.org/10.2355/isijinternational1966.27.570.
[2] S. Zaefferer, J. Ohlert, W. Bleck, A study of microstructure, transformation mechanisms and correlation between microstructure and mechanical properties of a low alloyed TRIP steel, Acta Mater. 52 (2004) 2765–2778, https://doi.org/10.1016/j.actamat.2004.02.044.
[3] Z.H. Cai, H. Ding, R.D.K. Misra, Z.Y. Ying, Austenite stability and deformation behavior in a cold-rolled transformation-induced plasticity steel with medium manganese content, Acta Mater. 84 (2015) 229–236, https://doi.org/10.1016/j.actamat.2014.10.052.
[4] S.O. Kruijver, L. Zhao, J. Sietsma, S.E. Offerman, N.H. Van Dijk, E.M. Lauridsen, L. Margulies, S. Grigull, H.F. Poulsen, S. Van Der Zwaag, In situ observations on the mechanical stability of austenite in TRIP-steel, J. Phys. IV Proc. 104 (2003) 499–502, https://doi.org/10.1051/jp4:20030131.
[5] M. Umemoto, W.S. Owen, Effects of austenitizing temperature and austenite grain size on the formation of athermal martensite in an iron-nickel and an iron-nickel-carbon alloy, Metall. Trans. 5 (1974) 2041–2046, https://doi.org/10.1007/BF02644497.
[6] E. Jimenez-Melero, N.H. Van Dijk, L. Zhao, J. Sietsma, S.E. Offerman, J.P. Wright, S. Van Der Zwaag, Characterization of individual retained austenite grains and

their stability in low-alloyed TRIP steels, Acta Mater. 55 (2007) 6713–6723, https://doi.org/10.1016/j.actamat.2007.08.040.
[7] B. He, On the factors governing austenite stability: intrinsic versus extrinsic, Materials (Basel) 13 (2020) 3440, https://doi.org/10.3390/ma13153440.
[8] T. Abe, K. Fujikura, R. Nagashima, N. Nakada, S. Yabu, Morphology dependence on mechanical stability of second-phase austenite in martensitic steels, ISIJ Int. 64 (2024) 421–429, https://doi.org/10.2355/isijinternational.ISIJINT-2023-112.
[9] R. Ueji, W. Gong, S. Harjo, T. Kawasaki, A. Shibata, Y. Kimura, T. Inoue, N. Tsuchida, Deformation-induced martensitic transformation at tensile and compressive deformations of bainitic steels with different carbon contents, ISIJ Int. 64 (2024) 459–465, https://doi.org/10.2355/isijinternational.ISIJINT-2023-253.
[10] R. Blondé, E. Jimenez-Melero, L. Zhao, J.P. Wright, E. Brück, S. Van Der Zwaag, N. H. Van Dijk, High-energy X-ray diffraction study on the temperature-dependent mechanical stability of retained austenite in low-alloyed TRIP steels, Acta Mater. 60 (2012) 565–577, https://doi.org/10.1016/j.actamat.2011.10.019.
[11] R. Ding, Y. Yao, B. Sun, G. Liu, J. He, T. Li, X. Wan, Z. Dai, D. Ponge, D. Raabe, C. Zhang, A. Godfrey, G. Miyamoto, T. Furuhara, Z. Yang, S. Van Der Zwaag, H. Chen, Chemical boundary engineering: a new route toward lean, ultrastrong yet ductile steels, Sci. Adv. 6 (2020) eaay1430, https://doi.org/10.1126/sciadv.aay1430.
[12] X. Wan, G. Liu, R. Ding, N. Nakada, Y.-W. Chai, Z. Yang, C. Zhang, H. Chen, Stabilizing austenite via a core-shell structure in the medium Mn steels, Scr. Mater. 166 (2019) 68–72, https://doi.org/10.1016/j.scriptamat.2019.03.015.
[13] S. Karewar, J. Sietsma, M.J. Santofimia, Effect of pre-existing defects in the parent fcc phase on atomistic mechanisms during the martensitic transformation in pure Fe: a molecular dynamics study, Acta Mater. 142 (2018) 71–81, https://doi.org/10.1016/j.actamat.2017.09.049.
[14] B. Wang, Y. Jiang, C. Xu, Phase transition in iron thin films containing coherent twin boundaries: a molecular dynamics approach, Materials (Basel) 13 (2020) 3631, https://doi.org/10.3390/ma13163631.
[15] Y. Jiao, W. Dan, W. Zhang, Effects of hydrogen on the deformation mechanism of face-centred cubic Fe–C single crystal with nanovoid: a molecular dynamics simulation, J. Alloys Compd. 870 (2021) 159330, https://doi.org/10.1016/j.jallcom.2021.159330.
[16] X.-Y. Zhou, H.-H. Wu, J. Zhang, S. Ye, T. Lookman, X. Mao, Unveiling the mechanism of carbon ordering and martensite tetragonality in Fe–C alloys via deep-potential molecular dynamics simulations, J. Mater. Sci. Technol. 223 (2025) 91–103, https://doi.org/10.1016/j.jmst.2024.10.020.
[17] J. Meiser, H. Urbassek, Ferrite-to-austenite and austenite-to-martensite phase transformations in the vicinity of a cementite particle: a molecular dynamics approach, Metals (Basel) 8 (2018) 837, https://doi.org/10.3390/met8100837.
[18] T. Shimokawa, K. Fujii, T. Niiyama, Atomic simulation study of the factors affecting nucleation in deformation-induced martensitic transformation in grains and at grain boundaries in pure iron, Acta Mater. 265 (2024) 119629, https://doi.org/10.1016/j.actamat.2023.119629.
[19] P.K. Tripathi, S. Karewar, Y.-C. Lo, S. Bhowmick, Role of interface morphology on the martensitic transformation in pure Fe, Materialia 16 (2021) 101085, https://doi.org/10.1016/j.mtla.2021.101085.
[20] F.-Z. Dai, W.-Z. Zhang, A simple method for constructing a reliable initial atomic configuration of a general interface for energy calculation, Model. Simul. Mater. Sci. Eng. 22 (2014) 035005, https://doi.org/10.1088/0965-0393/22/3/035005.
[21] A. Stukowski, Visualization and analysis of atomistic simulation data with OVITO–the open visualization tool, Model. Simul. Mater. Sci. Eng. 18 (2010) 015012, https://doi.org/10.1088/0965-0393/18/1/015012.
[22] P.M. Larsen, S. Schmidt, J. Schiøtz, Robust structural identification via polyhedral template matching, Model. Simul. Mater. Sci. Eng. 24 (2016) 055007, https://doi.org/10.1088/0965-0393/24/5/055007.
[23] S. Plimpton, Fast parallel algorithms for short- range molecular dynamics, J. Comput. Phys. 117 (1995) 44.
[24] C. Wu, B.-J. Lee, X. Su, Modified embedded-atom interatomic potential for Fe-Ni, Cr-Ni and Fe-Cr-Ni systems, Calphad 57 (2017) 98–106, https://doi.org/10.1016/j.calphad.2017.03.007.